Additively Manufactured IN718 Components with Wirelessly Powered and Interrogated Embedded Sensing

The material contained in this publication is based upon work supported by the Department of Energy under Award Number DE-FE0012299; through a project entitled, *ATOMeS: Additive Topology Optimized Manufacturing with embedded Sensing*.

Additively Manufactured IN718 Components with Wirelessly Powered and Interrogated Embedded Sensing

P. Attridge, S. Bajekal, M. Klecka, X. Wu, S. Savulak, D. Viens,
M. Carey, R. Gosselin, J. Miano, J. Needham, W. Rioux, J. Zacchio, and J. Mantese[†]
United Technologies Research Center, East Hartford, CT 06118

Richard Dunst and D. Straub
National Energy Technology Laboratory, Pittsburgh, PA 15236

Abstract

A methodology is described for embedding commercial-off-the-shelf sensors together with wireless communication and power circuit elements using direct laser metal sintered additively manufactured components. Physics based models of the additive manufacturing processes and sensor/wireless level performance models guided the design and embedment processes. A combination of cold spray deposition and laser engineered net shaping was used to fashion the transmitter/receiving elements and embed the sensors, thereby providing environmental protection and component robustness/survivability for harsh conditions. By design, this complement of analog and digital sensors were wirelessly powered and interrogated using a health and utilization monitoring system; enabling real-time, *in situ* prognostics and diagnostics.

Keywords: additive manufacturing, DMLS, LENS™, cold spray, prognostics and health monitoring, wireless, embedded sensing, IoT, aerospace

[†]Author to whom correspondence should be sent: mantesjv@utrc.utc.com

1.1 Introduction

The failure of wired sensing elements continues to be a significant source of no fault found (NFF) in systems ranging from automotive to aerospace[1-5]. While there are many reasons for these failures, electrical contacts have been identified as one of the principal failure modes in nearly all systems requiring an extended wiring harness connected to a system of sensors, microprocessors, microcontrollers, or line replaceable units. Concomitantly, however, the use of integrated sensing and the extension of the internet of things (IoT) to commercial building, automotive, biomedical, health, aerospace and defense systems implies a proliferation of sensing systems so as to enable: closed loop control, prognostics and health monitoring (PHM), condition based maintenance, and the collection of big data to facilitate holistic system-of-systems level monitoring[6-13]. In this paper, additively manufactured (AM) processes will be shown as unlikely facilitators for extending the IoT to physically demanding environments where conventional packaging is inadequate for sensor survival. In particular, a methodology is described for embedding a wireless sensing network into AM components. The methodology is inherently meant to be AM process agnostic; though in this work we primarily use direct metal laser sintering (DMLS), metal cold spray (CS), and laser engineered net shaping (LENS^{TM}) processes to demonstrate the approach.

To specifically address the nocent issues associated with "wired" sensors, the sensing elements in this work are powered and interrogated through near field radio frequency (RF) radiation supplied by an induction coil with enhanced performance facilitated by magnetic focusing elements. We confine our efforts to the use of readily available commercial-off-the-shelf (COTS) sensors and integrated circuits to create the wireless power and signal sensor network. The methodology was heavily guided by finite element physics based modeling to

ensure: (1) The structural and thermal integrity of the host component was unaltered. (2) The survivability of the sensing elements throughout the embedment and operating environments. (3) The fidelity of the inputs and outputs (I/O) to and from the sensing elements (analog and/or digital) to a "Reader". (4) Sufficient wireless power was transferred, and locally stored, on the "Tag" side of the sensing suite so as to power the microprocessor, memory elements, sensors, and receiver/transmitter.

It is important to state at the outset of this paper that the primary intent of this effort was to **create the methodology for holistically integrating sensing, communication, and power into an otherwise electrically passive structural component without degrading either its functionality or life**. The creations of new AM processes or new methods for fabricating sensing elements were not primary goals of this research. Indeed, this research effort specifically made the use of COTS components and well-developed AM processes a tenet of the project; thereby permitting us to exploit the rich palette of previously matured technologies in addition to facilitating transfer of our findings to the greater technical community.

2.1 Materials and Methods

Systems of systems that exploit interconnected networks of sensor nodes for self-diagnostics and prognostics continue to proliferate, finding applications in: integrated buildings, electrical grid control, health care, biomedical systems, traffic management, and manufacturing process control[6-13]. When the outputs of such a sensor network are aggregated into health and utilization monitoring systems (HUMS), large data analysis can often yield trending information that can recognize premature failure or manufacturing defects, or (conversely) allow for a delay in removal of a component or tear down of a system that might be otherwise mandated in schedule

based maintenance protocols[14-16]. However, the extension of the IoT to systems of components that experience severe environmental demands remains problematic, especially those that primarily utilize wiring harnesses to provide local power and to send and extract signals and commands. Electrical interconnects fail at a significant rate in even the most benign environments[1,4], and therefore their use becomes a serious obstacle in settings where temperature and operational gases are deleterious to network integrity[2.3.5].

Figure 1a, for example, shows a FT4000^{TM} ground based gas turbine system, consisting of compression and turbine stages. The FT4000^{TM} is a derivative of an aero engine, however, without the fan; the latter of which is used to create propulsion in flight. Such generators, and their much larger counterparts, are often run near open loop without significant real time feedback controls due to concerns related to sensor failure and system downtime. Consequently, they are often perform at less than full efficiency and experience unplanned downtime[9-12]. Figure 1b shows a conceptual design of an instrumented FT4000^{TM} inlet guide vane (IGV) with wireless signal and power to a suite of embedded sensors as an evolution of the IoTs to systems subjected to extreme environmental conditions. While this effort does not succeed in creating a full scale additively manufactured IGV due to its size (which is currently beyond most DMLS manufacturing beds), an IGV prototype has been designed and fabricated with all the essential sensing and communication features shown.

Figure 2 describes a general methodology for creating a sensor network in instrumented "Smart Parts" connected to a health and utilization monitoring system by: (1) First articulating the Concept of Operation (ConOps) and Key Parameters of Interest (KPIs) for the system. As part of this effort one must also determine what sensing elements are required to support the ConOps that achieves the desired performance golas. (2) Creation of materials, manufacturing,

and sensing requirements documents. (3) Notional selection of the sensors, materials and manufacturing processes consistent with the requirements to realize the structure of interest and the sensing capabilities. (4) Optimization of the structure topology and manufacturing processes to ensure the sensors and wireless network work properly in the control environment AND the component continues to be functional without any diminution in life or performance.

While a full scale fabrication and testing of an IGV would have been highly desirable, the actual dimensions of the structure shown schematically in Fig. 1b are currently prohibitively large (>50cm in length) for most DMLS powder bed processes qualified at UTC. Consequently, a reduced dimensional structure was designed to capture the salient features of an instrumented IGV, Fig. 3. As shown schematically, this structure was designed to have on board: (1) Three thermocouple sensors, including, two sensors to capture the static temperature flow of the gas impinging along the leading edge of the vane, and one dynamic temperature sensor along the length of the surrogate vane. The purpose of this structure was to act as an *in situ* thermocouple "rake" often used in aerodynamic test configurations to assess flow rates, pressure drop, and thrust[17,18]. (2) An onboard 3-axis accelerometer, the workhorse of a typical HUMS prognostics and health monitoring system[13-16]. (3) A solid state temperature sensor for monitoring the local temperature near the silicon ICs and to act as reference for the three embedded thermocouples. (4) Castellated features for a variable reluctance angular position sensor. As will be described later, DMLS IN718 is non-magnetic; thus to provide a target structure for the embedded Hall sensors, 410 stainless steel (410SS) had to be cold sprayed onto the preform to create a structure that would enable accurate angle determination.

In addition to the features described above, cooling channels were provided to ensure that the maximum temperature of the interior structure where the electronics was housed never exceeded

50°C even when the surrogate vane was exposed to 600°C flowing air. The solid state temperature sensor described above was particularly useful in adjusting the supplemental cooling flow rate real time as it could be monitored through the health and utilization monitoring system. Detailed thermal analysis was performed (not shown here) using COMSOL™ and verified at the National Energy Technology Laboratory (NETL) test facilities using a reference thermocouple attached to the surrogate vane. In all respects, the thermal-mechanical analysis and experiments were consistent as required by the methodology outlined in Fig. 2.

Figure 4a shows a block diagram of the components used to provide wireless signal and power. Specifically, the electronics for this effort were comprised of two separate circuit assemblies. One assembly located inside the stationary shaft, the "Reader" was powered by an external DC power supply. It had a UART/USB link used to transmit data to an external Data Acquisition (DAQ) system. Directly opposite the Reader, a "Tag" was located on the vane side of the shaft. The Tag was powered as well as queried for data via RF transmissions from the Reader and had no physical connection to the Reader. Unlike an IGV comprising a PW FT4000™ generator the portion of the shaft with the Reader was made to rotate while the vane remained stationary.

The Reader was controlled by a Texas Instruments MSP430FR5949 16 MHz Ultra Low Power Microcontroller running a Finite State Machine (FSM) written in C. The FSM interfaces with a Texas Instruments TMS3705 Base Station IC to alternate between transmitting a charge to the probe, and requesting data from the Tag via the RF link. The Reader had circuitry on board to perform analog to digital conversion of voltages from the two Hall effect sensors in the shaft (see Fig. 5a) that are positioned to sense the castellations in the vane side of the shaft, allowing the Reader to determine the angular orientation of the vane.

The Tag was managed by a separate MSP430FR5949 microcontroller with interface to a Texas Instruments TMS37157 Transponder IC. Sensing circuitry on the Tag includes a local analog to digital conversion IC to read an onboard thermistor (as a temperature reference) and the three thermocouples in the vane. Also included is a digital MEMS accelerometer IC indicating acceleration of the Tag PCB in the X, Y and Z axes.

The TMS3705/37157 chipset is intended for RFID applications, and employs a half-duplex communication architecture. One complete power and communication cycle essentially incudes three steps: (1) The Tag storage capacitors are charged through the RF link, during which time no communication can occur. (2) The Reader submits a sensor data request command using Amplitude Shift Keying (ASK) at a carrier frequency of 134.5kHz. (3) The Tag responds with three data commands using Frequency Shift Keying (FSK) at 123kHz and 134.2kHz. FSK is achieved by energizing an inductor-capacitor (LC) resonant tank and varying the capacitor between two discrete values. The Tag-side coil of the RF link coil-set represents approximately 33% of the total resonant inductance. The Q of the total resonant inductance determines the amount of time the FSK link can operate, and must be greater than 30 to allow a complete downlink command to complete. The first two data commands include four bytes each and contain ADC data for the thermocouples and thermistor. The last data command includes six bytes representing accelerometer data. This cycle has a repetition rate of approximately 1Hz. Communication commands can also take advantage of a unique code factory-programmed into the TMS37157, giving the Tag an inimitable identifier.

Given that the Tag draws all its power from the Reader through the RF connection, and the cross sectional area available for the magnetic link is severely limited by the small internal diameter (14mm) of the ferrite, only extremely energy efficient circuit elements were considered.

Based on initial electromagnetic simulations and trials, a total active power budget of just 3mW was established for all four functions on the Tag. Careful COTS part selection led to a suite of components with full and quiescent power consumption totals of 2.4mW and 1.7mW, respectively.

Detailed electromagnetic models were used throughout this effort as previously described relative to the methodology of Fig. 2. These analyses were necessary to ensure that sufficient power transfer occurred between Reader and Tag. Moreover, the data rates, dropout, and signal to noise, all critically depended upon maintaining good flux coupling between the Reader and Tag. Electromagnetic coupling between the Reader and Tag was achieved with two separate coils wound on 11mm diameter ferrite p-cores. The Reader coil used 123 turns of 38AWG enamel-coated wire, achieving an inductance of 378uH and a Q of 45. The Probe coil also used 38AWG wire, but had 181 turns for an inductance of 800uH and a Q of 37. Figure 4b shows the simulation model of the p-cores and the coils developed in Maxwell^{TM}. The electromagnetic analysis helped to evaluate the coupling factors between the Reader and Tag coils at different air gaps, as well as the inductances of each coil. The flux lines of the electromagnetic field generated by the Reader coil are shown in Figure 4c. The flux coupling and hence voltage that appeared upon the Tag coil was a function of the skin depth, $\delta=(2/\omega\sigma\mu)^{1/2}$, of the metal interposed between the two cores. Here, ω is the angular frequency in radians, σ is the electrical conductivity of the metal, and μ is the permeability of the interposed metal. The ferrites were used to provide superior magnetic coupling between the two cores; whereas the interposed metal was used to environmentally shield the Reader and Tag electronics. The skin depth of the interposed metal could be dramatically increased (by as much as 10^7 times) by incorporating SiC or other high resistivity dielectric into the cold sprayed IN718 alloy that was used to encapsulate

the two coils. We found that even with as much as 0.3 cm of interposed metal, the two coils were sufficiently coupled to provide adequate power and signal between the Tag and Reader. For the results described below, we determined that the encapsulation was not required and thus only a small air gap was used to separate the coils.

Control or diagnostic systems traditionally make use of at least three physical/thermodynamic quantities when interrogating a system's status: a local temperature, a physical position, and positional velocity/accelerations. The surrogate IGV has two forms of integrated temperature sensing, a simple thermistor located on the Tab board structure show in Fig. 4a, and type K thermocouples located along the leading edge and face of the test structure.

Extensive thermal-mechanical modelling guided the thermocouple embedding process per the methodology described in Fig. 2. Although a UTC specified DMLS process was used to fabricate the bulk of the Inconel alloy (IN718) test structure, the encapsulation of the thermocouples was accomplished using an IN718 via the laser-powder deposition LENS^{TM} process. The dimensions of the pre-fabricated "pocket' were determined using physics based modeling such that the process would not result in catastrophic melting of the inner electrodes of the thermocouples though did melt the IN718 thermocouple sheaths. The COMSOL^{TM} modelling considered various channel widths, depths, and aspect ratios as well as LENS^{TM} feeds, speeds, spot size, and power levels. Figure 5a represents a typical simulation use to compare the effects of LENS^{TM} power and focus during the embedment of the thermocouples. Note that for a laser power of approximately 100W, the melt pool of the LENS^{TM} deposited IN718 just exceeds the melting point of the material, enabling partial melting of the sheath, Fib. 5b, and thus good mechanical bonding. Modifications to the placement of the thermocouple by rounding the base

of the groove and press fitting followed by tack welding ultimately resulted in a superior embedding process.

After the three thermocouples were embedded into the IN718 test structure, the surfaces were ground smooth along the leading edge and face. Subsequently, the three thermocouples were tested; see Table 1, at room temperature, in an ice bath, and in boiling water against a reference type K thermocouple. Two additional calibration points were captured as transient readings. Note that the embedding process did not substantially alter the response of the embedded thermocouples, as they all read to within 2°C of each other.

The inlet guide vane of a ground based natural gas turbine system must rotate about a set point to adjust for optimal turbine performance and greatest energy generation with minimum fuel consumption. The angular swing of an IGV is typically much less than $\pm$45° and is set using a mechanical actuator linked through a unison ring. Angular placement is determined with the use of a linear actuator and linear variable differential transformer (LVDT) which acts as a displacement sensor. Unfortunately, the stack up errors in the various linkage arrangements can lead to miss-positioning of the IGV by up to a few degrees, depending upon the age of the turbine system and the tolerances employed in its design and manufacture. Miss-positioning of the IGV ultimately results in reduced turbine generator performance, and is mirrored in aero engines. Thus to mitigate this deficiency, an angular position sensor was designed into the test structure so as to accurately read angular position directly at the vane, instead of through linkages back to an LVDT.

Figure 6a is an electromagnetic model of an angular position sensor. It is based upon an automotive variable reluctance design[19,20]. The IN718 test structure was designed with castellated features, upon which 410SS was cold sprayed and then back-machined smooth, Fig.

6b. The cold spray of 410SS into the valleys of the IN718 castellated features and on its ensured that the magnetic flux from the magnet backing the Hall sensors would be channeled through the Hall sensor. Deposition of the 410SS was accomplished using a high pressure cold spray system, operated with helium process gas at 40 bar pressure (580 psi) and at 450°C inlet temperature. The system was robotically controlled, including a rotary part manipulator used to deposit on the outer surface of the castellated structure while maintaining a 1-inch standoff distance for the cold spray nozzle. The 410SS powder was injected upstream of the nozzle in a pre-chamber, allowing preheating of the powder to improve the deposition efficiency and deposit density.

To further augment the performance of the angular position sensor, high permeability alnico alloy magnetic focusing lens were added to the Hall sensors to further concentrate the magnetic flux, see Fig. 6a. Lastly, a second Hall sensor with castellation 180° out of phase, see Fig. 6a and Fig. 6b, were AM'ed onto the IN718 with cold sprayed 410SS, thereby allowing the sensor to operate in differential mode, and thus achieve greater angular resolution. Testing of the angular position sensor, see Results and Conclusions section, was done with an external instrument grade encoder to determine sensor resolution.

3.1 Results and Conclusions

Figure 7 shows the IN718 test structure made using a DMLS powder bed process. A tooling plate was immersed in a bed of metallic powder and a 2D surface of the powder was laser scanned, resulting in localized powder fusion. The tooling plate was lowered into the powder bed, and a fresh layer of powder was prepared for the subsequent scan. The part was formed by successively stacking XY planar slices to grow the structure in the Z direction. In this case, the part Z axis was collinear with the cylindrical body of the vane.

Overhangs such as the vane platform were supported by light "scaffolding" which provided anchoring down to the tooling plate. This temporary structure was easily removed after fabrication by either wire Electron Discharge Machining (EDM) or with a conventional abrasive/cutting saw. Either process was followed by finishing. Unfused powder trapped inside of internal cavities was removed through passageways by vibratory agitation. This latter process had to be done prior to any heat treating processes or partial fusion would occur, impeding the cleanup.

The embedded thermocouples (TC's) were subsequently installed into the grooved features designed into the vane. The TC's were welded into place and encapsulated using a full 3D LENS^{TM} process. This latter process was conducted in an inert atmosphere enclosure, using IN718 powder matching the composition of the base DMLS substrate.

The IGV surrogate was tested at the NETL high temperature aerothermal test facility. This test facility includes a high-pressure combustor and an optically accessible flow channel located downstream of the swirl stabilized natural gas combustor. This facility has been used to study film cooling performance at high temperature and high pressure conditions and details can be found elsewhere[21,22].

In this study, the prototype assembly interfaced with the existing heat transfer test section and flow channel. As shown in Fig. 3 and Fig. 8a, the test structure was positioned into the hot gas path exiting the combustor and the Reader assembly was located in the cooling air plenum region. Figures 8b and 8c show the system architecture and physical layout, respectively of the test setup at the NETL facility. Situated next to the test structure were the HUMs computer and two DC power supplies for the Reader assembly, DAQ module, and the actuator. Data collected by the Reader and DAQ module was transmitted to the HUMs computer via a USB connection

which was used a synchronous serial protocol at a 115.2kbps baud rate with eight data bits, one stop bit and no flow control or parity. These transmissions were read by a LabVIEW program that presents all of the data to the user via a GUI in real time, and logs all data to a text file at a rate of approximately 20 samples per second. The recording rate was calculated to ensure the highest fidelity and still allow reasonable file sizes during long logging periods. To ensure operator safety, the HUMs computer was connected to an Ethernet switch and all interactions were performed through a laptop located in the test rig control room, connected to the same Ethernet switch.

A metered supply of cooling air flows was channeled into the cooling plenum and through the platform region of the vane. Apart from the platform cooling, no other cooling was provided to the vane. Following a short preheat period in which the temperature readings were collected, cooling air flows adjusted, and pressure drop measurements verified; combustion was initiated. After ignition, the hot gas path temperature increased rapidly to approximately 500°C. The pilot fuel was adjusted to achieve the target centerline gas temperature of 620°C near the vane, see Fig. 9e. After a period of time, the combustor was shut down and the centerline gas temperature decreased quickly from 620°C to approximately 120°C.

Figures 9a-9d show the data wirelessly acquired from the sensor suite embedded in the surrogate IGV and transferred to the HUMS system during the temperature profile shown in Fig. 9e. The outputs from each of the sensors were time stamped using the architecture of Fig. 8b, thereby allowing any anomaly detection at peak temperature excursion. Figure 9a (the solid state temperature anchored *in situ* on the Tag PCB) indicates that the electronic component temperatures were maintained below 100°C; a result of the forced cooling through the channels designed into the component. During this same temperature cycling, the Reader was swept

repeatedly through 90° of rotation and back as determined by the optical encoder affixed to the Reader stock. Concurrently, the Hall effect sensor pairs were interrogated to yield an angular position based upon their variable reluctance. Detailed analysis and comparison against the instrument grade angular position sensor indicated that the additively embedded angular position sensor allowed placement to better than 0.1° when utilizing the differential between the two Hall sensors. Figure 9c shows the output of two channels of the accelerometer. As the flow system had very little vibrational noise, the readings are relatively uninteresting as they show the steady state acceleration of gravity along the axis aligned along the probe, and no net acceleration otherwise. Finally, Fig. 9d shows two thermocouple outputs during system temperature ramp. TC2 was normal (leading edge) to the gas flow and represents a kinematically "static" measurement; whereas the temperature read by TC1 was along the face of the test structure.

The outputs from the sensor suite were ultimately accumulated into a health and utilization monitoring system (HUMs) similar to that which was used to collect data and forecast failures in aerospace systems; including both fixed wing and rotorcrafts. Such systems have been used to provide system health prognostication, and resulted in the successful transition of some protocols from schedule based to system based maintenance. The resulting savings in cost and unscheduled down-time can be considerable for aero and land based turbine systems. The creation of a "Smart Part" compatible with demanding environment requirements and interfacial to a HUMS system is a significant step toward extending the IoT's to non-benign application spaces.

Although not explored extensively in this paper, was how embedded intelligence and part identification could potentially impact supply chain management. Indeed, substantial saving related to inventory management[23,24] can be an ancillary benefit of creating a component with individualized onboard tracking ability. Moreover, component individualization and tracking can

potentially prevent: the nefarious introduction of defects during additive manufacturing, the use of manufacture rejected components, the recycling of end-of-life parts, and the introduction of counterfeit components into the supply chain[25-33].

4.1 Peer Review Response

On August 24, 2015, peer review of this Department of Energy sponsored effort was conducted. The purpose of this rigorous assessment was to identify and delineate the: methodology, milestones, timing, and likely shortfalls of the project so as to provide mid-course correction (if necessary) to optimize the technical accomplishment of the performers. To that end, the peer review committee suggested the following actions:

1. **Request:** The project team was encouraged to pursue refereed publications to disseminate knowledge gained in this project to the technical community.

   Action: The materials contained in this final report were submitted in total as a holistic review paper to the *Journal of Additive Manufacturing* in April, 2017. The project team is awaiting a response from the editor as to its acceptance.

2. Request: The project team was urged to conduct longer-term tests at 1100 °F to assess the longer-term performance of the embedded device and the surface covering technique. The test could be simpler, such as testing samples of the material and thermocouple at the desired temperature, to assess longer-term performance.

   Action: Unfortunately, the project team was not able to complete this task. There were significant difficulties encountered in designing, fabricating, and executing the wireless signal and power protocols. As identified prior to initiating the effort, this risk was the most difficult to retire. Consequently, this WBS element consumed resources meant for

long term testing, and thus insufficient funds remained to address this concern as the project neared its completion.

3. **Request:** The project team was encouraged to articulate the pathways towards achieving different TRLs with regard to each sensor type (i.e., thermocouple, solid-state temperature sensor, accelerometer), material interactions between the sensor and the base materials during the embedding process, mechanical testing, and other aspects of sensor embedding (e.g., adequate sensor lifetimes, thermal cycling durability, etc.). The team was asked to examine the mechanical characteristics (qualification) of the structure modified with the sensor material to ensure adequate mechanical performance.

   Action: The project team was able to transfer their key findings to UTC business units, who are funding an effort to mature the technology to TRL6 and beyond to production. The business unit has engaged outside vendors to realize key components, and has placed the technology on its planning roadmap. Most impressively, the team has already demonstrated a >>10X improvement in data bandwidth, a >>10X improvement in communication and power transfer, and a path to 500°C compatible technology.

5.1 Acknowledgments

The authors are indebted to Andrew Consiglio, David Furrer, Charles Haldeman, Kurt Sobanski, and Bruce Wood of Pratt & Whitney (PW) for discussions related to additive manufacturing, instrumentation for aerospace systems and potential PW applications and off-ramps; Michael Lynch of UTC Aerospace Systems for guidance related to harsh environment wireless power and signal networks and aerospace protocols and regulations; Craig Carder of C3 Medical Device Consulting, LLC for custom MSP coding of the RF and DAQ links; and Gary

Hunter of NASA Glenn Research Center; Sydni Credle, Paul Ohodnicki and Ben Chorpening of the National Energy Technology Laboratory for their many helpful discussions relating to packaging, sensing, testing in extreme environments, and technology manufacturing readiness. The authors also wish to thank Jeff Crandall of the Connecticut Center for Advanced Manufacturing (CCAT) for assisting us with the LENS^{TM} processing.

Finally, the Department of Energy is also gratefully acknowledged as the material contained in this publication is based upon work supported by the Department of Energy under Award Number DE-FE0012299; through a project entitled, *ATOMeS: Additive Topology Optimized Manufacturing with embedded Sensing*.

References

1. The Reliability of Electronically Controlled Systems on Vehicles, I. Knight, A. Eaton, and D. Whitehead, PR/SE/101/00, April, 2001.

2. Managing Electrical Connection Systems and Wire Integrity on Legacy Aerospace Vehicles, S.J. Sullivan, G.A. Slenski, www.mitremai.com/.../NASA_Aging_Aircraft_Workshop_Paper.pdf

3. Aviation Wiring Networks Fault Modeling and Simulation Based on Relectometry, X. Shi, C. Liu, and Z. Yang, International Conference on Computer, Communications and Information Technology (CCIT 2014), pgs. 1-4.

4. **Electrical Contacts**, P. Slade editor, 2nd Edition, CRC Press, Taylor and Francis 2014, Chapter 1, pgs. 3-11.

5. No Fault Found: The Search for the Root Cause, S. Khan and I.K Jennions, SAE International, 2015, pgs.

6. Review of Cyber-physical Systems, Y Liu, Y. Peng, B. Wang, S. Yao, and Z. Liu, IEEE Jour. Automatica Sinica, Vol. **4**, No. 1, January 2017, pgs. 27-40.

7. A Survey of Intelligent Control and Health Management Technologies for Aircraft Propulsion Systems, J.S. Litt and D.L. Simon, R. Millar, A. Behbahani, A. Bajwa, D.T. Jensen, NASA/TM-2005-213633, May 2005, pgs. 1-22.

8. Low cost wireless sensors for building monitoring systems, https://energy.gov/sites/prod/files/2014/10/f18/emt67_kuruganti_042414.pdf

9. Advanced Sensors and Monitoring & Diagnostics (M&D) for Gas Turbines, V.V. Vadami, GE Energy Engineering, http://www.stanford.edu/class/ee392n/lecture/apr24/vvd_ge.html

10. Online Monitoring of Gas Turbine Power Plants, H. Brummel, D.H. LeMieux, M. Voigt, P.J. Zombo, pgs. 1-24, http://www.energy.siemens.com/us/pool/hq/energy-topics/pdfs/en/gas-turbines-power-plants/4_Online_Monitoring_of_Gas.pdf

11. Opportunities for Advanced Sensors for Condition Monitoring of Gas Turbines, R.M. Cotgrove and M.I. Wood, Opp. Adv. Int. Power Generation, Mar. 1996, 119-124.

12. Advanced Turbine Systems Sensors and Controls Needs Assessment Study Final Report, R.L. Anderson, D.N. Fry, and J.A. McEvers, ONRL Inter. Rpt., ORNL/TM-13335, Feb. 1997.

13. Model-Based Sensor Placement for Component Condition Monitoring and System Fault Diagnosis in Fossil Energy Systems, R. Rengasamy, http://www.netl.doe.gov/publications/factsheets/project/FE0005749.pdf

14. HUMS/MMIS as an Aviation Combat Multiplier, T.M. Somers, R.K. Bonino, B.R. Cleave, J.D. Wright, H.S. Kunselman, R.L. Medina-Santiago, Presented at the American Helicopter Society 63rd, Annual Forum, Virginia Beach, VA, May 1-3, 2007.

15. US Navy Roadmap to Structural Health and Usage Monitoring-The Present and Future, S. Maley, J. Plets, and N.D. Phan, NAVAIR Public Release 07-065, 2007.

16. Structural Health Monitoring for Aircraft: Viable Inspection Tool or Passing Fancy?, D. Roach, http://airlines.org/wp-content/uploads/2016/11/9_28_930.pdf .

17. Design and Development of an F/A-18 Inlet Distortion Rake: A Cost and Time Saving Solution, A.J. Yuhas, R.J. Ray, R.R. Burley, W.G. Steenken, L. Lechtenberg, and D. Thornton, NASA Technical Memorandum 4722, 1995, pgs.1-22.

18. Development of Full Annular Combustor for Small Aircraft Jet Engine in JAXA TECHCLEAN Project, M. Makida, H. Yamada, T. Yamamoto, 26th Inter. Cong. Of the Aero. Sci., ICAS 2010 Proceedings, pgs. 1-9.

19. **Sensors and Actuators in Mechatronics**, A.M. Pawlak, Taylor and Francis, CRC Press, 2007, pgs. 27-76.

20. **Automotive Electronics Handbook**, R.K. Jurgen, McGraw Hill, 2nd Edition, Copyright 1999, pgs. 3.1-3.18 and 7.1-7.8.

21. Straub, D. L., Sidwell, T. G., Casleton, K. H., Alvin, M. A., Chien, S., and Chyu, M. K., 2012, "High Temperature Film Cooling Test Facility And Preliminary Test Results," ASME Paper GT2012-69767.

22. Lawson, S. A., Straub, D. L., Beer, S., Casleton, K. H., and Sidwell, T., 2013, "Direct Measurements Of Overall Effectiveness And Heat Flux On A Film Cooled Test Article At High Temperatures And Pressures," ASME 2013GT-94685.

23. Excellence in Cost Management: A New Era for Aerospace, V. Marya, M. Parkins, K. Sachs, C. Shaw, McKinsey&Co., Aug. 2014

24. You could buy an Australian island for what the Pentagon says it would cost to take inventory — of one item, Lauren Chadwick, http://www.publicintegrity.org/2016/03/15/19428/you-could-buy-australian-island-what-pentagon-says-it-would-cost-take-inventory-one

25. Counterfeit Parts: Protecting the DoD Supply Chain, J. Weed, WSTIAC Quarterly, Vol. 10, No. 1, http://wstiac.alionscience.com/quarterly, 2010.

26. Counterfeit Parts: Increasing Awareness and Developing Countermeasures, M. Blakey, Aerospace Industries Association, March 2011.

27. Counterfeit Aircraft and Avionic Parts, Rear Adm. C. Parry CBE, www.accelus.thomsonreuters.com , 2012.

28. NAVSEA: Non-Electronic (Mechanical) Counterfeit Materials, John Butler, Director of Supplier Product Quality Control, NAVSEA Memorandum 2013-0537.

29. Construction Supply Chain Integrity: Mitigating the Counterfeit Threat, R. E. Minchin, R.C. Walters, F. Dongping, P. Jiayi; Bangkok, Thailand, Nov. 4-5, 2014.

30. Counterfeit Parts: DoD Needs to Improve Reporting and Oversight to Reduce Supply Chain Risk, GAO-16-236, Report to Congressional Committees, February 2016.

31. The Cost of Counterfeit Metal Construction Materials Corrugated Metals, Inc. 2013.

32. U.S. Space Industrial Base: Counterfeit Incidents and Protocols, Jason Bolton, June 12, 2015.

33. The Counterfeit Parts and Materials Challenge, Boeing – Phantom Works, L. Condra, T. Marino, A. Mester, B. Procarione, B. Scofield, 15th Annual CQSDI Cape Canaveral, FL, March 26-27, 2008.

Figure Captions

Figure 1:

(a) Commercial FT4000^{TM} industrial ground based turbine electrical generator; a derivative of an aero engine showing the compression and turbine stages without the fan, which is used for propulsion.

(b) Schematic of the FT4000^{TM} inlet guide vane instrumented with wireless signal and power to provide static and dynamic temperature measurements ("rake" design), in addition to vibratory and angular position readings.

Figure 2:

Diagram of the process flow used to design and fabricate a wirelessly powered and interrogated component with an embedded sensor network. While of general applicability, this process specifically facilitates the additive manufacturing of components that experience harsh environments where contact failure can be fatal to the network. By design, only commercial off the shelf sensing and wireless IC components are utilized. The numbers in the figure refer to the goals of each step as described in the paper proper.

Figure 3:

Schematic of the test structures employed in this work that captures the salient features of an inlet guide vane with embedded sensing and wireless signal and power.

Figure 4:

(a) Block diagram of the components used to achieve wireless signal and power sensing and communication.

(b) "Reader" and "Tag" configuration with p-cores for magnetic field intensification.

(c) Magnetic field intensity at the "Tag" side of a pair of inductively coupled coils. Specially designed ferrite cores act as magnetic field concentrators on the "Tag" and "Reader" side. Each additively manufactured component has a unique identity due to the assignment of an individualized RFID address.

Figure 5:

(a) Finite element thermal-mechanical analysis created to capture the thermal excursions during the thermocouple embedding process using the deposition of IN718 with the LENS^{TM} process. The study was done to ensure that the temperatures the thermocouples were exposed to during the embedding process just barely melted the thermocouple sheath.

(b) Cross sectional image of a test thermocouple showing the sheath melt while simultaneously confirming that the two thermocouple leads remain intact.

Figure 6:

(a) Schematic of the dual angular position sensors showing the magnetic flux at anti-positions of the castellated structure.

(b) Detailed photograph showing an IN718 form after the cold spray deposition of 410 stainless steel and post machining.

Figure 7:

Image of an additively manufactured component consisting of an IN718 Direct Metal Laser Sintered body and test struture prior to Laser Engineered Net Shaping to embed the thermocouples for static and kinetic temperature sensing; and prior to 410 stainless steel Cold Spray on the castellated structure to enable angular position sensing - specifically for use with Hall sensors in a variable reluctance configuration.

Figure 8:

(a) Schematic of the NETL test setup. Unlike a real inlet guide vane configuration; here, the vane (Tag side) is stationary and the Reader side is rotated.

(b) Schematic of the instrumentation layout for the NETL Morgantown, WV tests.

(c) Photograph of the test setup at NETL.

Figure 9:

Sensor outputs during thermal ramp and hold (a) Solid state thermistor used as the junction reference and to ensure that the temperature excursions of the electronics were less than 125°C. (b) Angular position as measured by Hall sensors and reference sensor during $\pm$90° rotations while temperature ramping. The inset shows the output from one sensor during a single 90° rotation at peak temperature. (c) Output of the embedded accelerometer along axes parallel and orthogonal to the gravitational force vector. (d) Thermocouple output during system temperature ramp. TC2 was normal to the gas flow "static" measurement. TC1 was embedded along the face of the test structure. (e) Thermal profile (using a reference thermocouple) in the flow stream. **Nota Bene:** The difference in temperature readings between the embedded thermocouple and reference is due to the fact that forced cooling air was injected through the body of the test structure to ensure proper electronics cooling; resulting in reduced temperature at the test structure.

Table Captions

Table 1:

Comparison of the readout potentials and computed temperatures for a reference thermocouple and the three embedded thermocouple devices; readings were taken in ice, at room temperature, and in boiling water. In addition, transient calibration points were also taken between room temperature and 100°C. Note that variations between the reference sensor and readings taken from the embedded sensors are approximately less than 2°C after the LENS^{TM}-based embedding and post machining processes.

FIGURE 1a

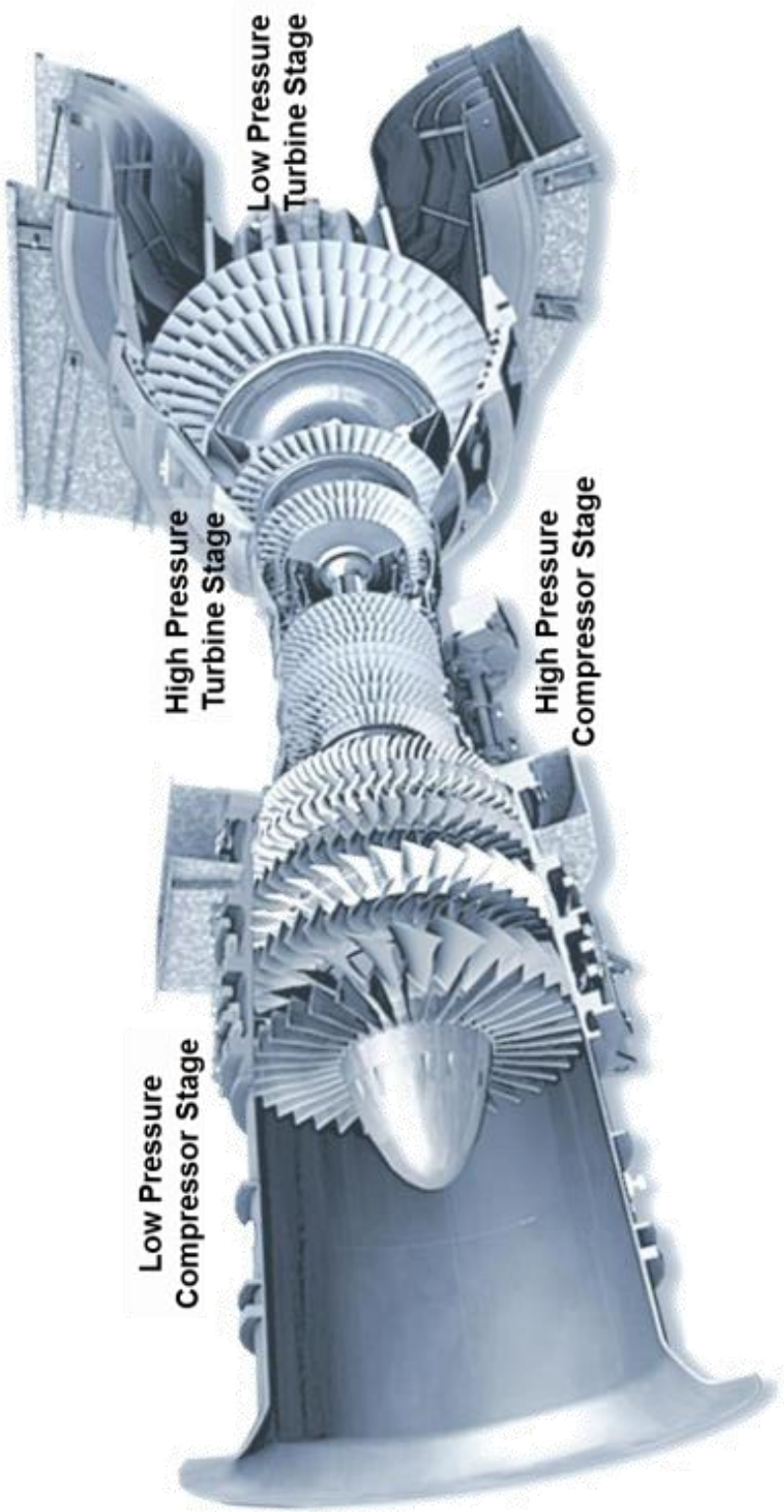
Low Pressure Turbine Stage
High Pressure Turbine Stage
High Pressure Compressor Stage
Low Pressure Compressor Stage

FIGURE 1b

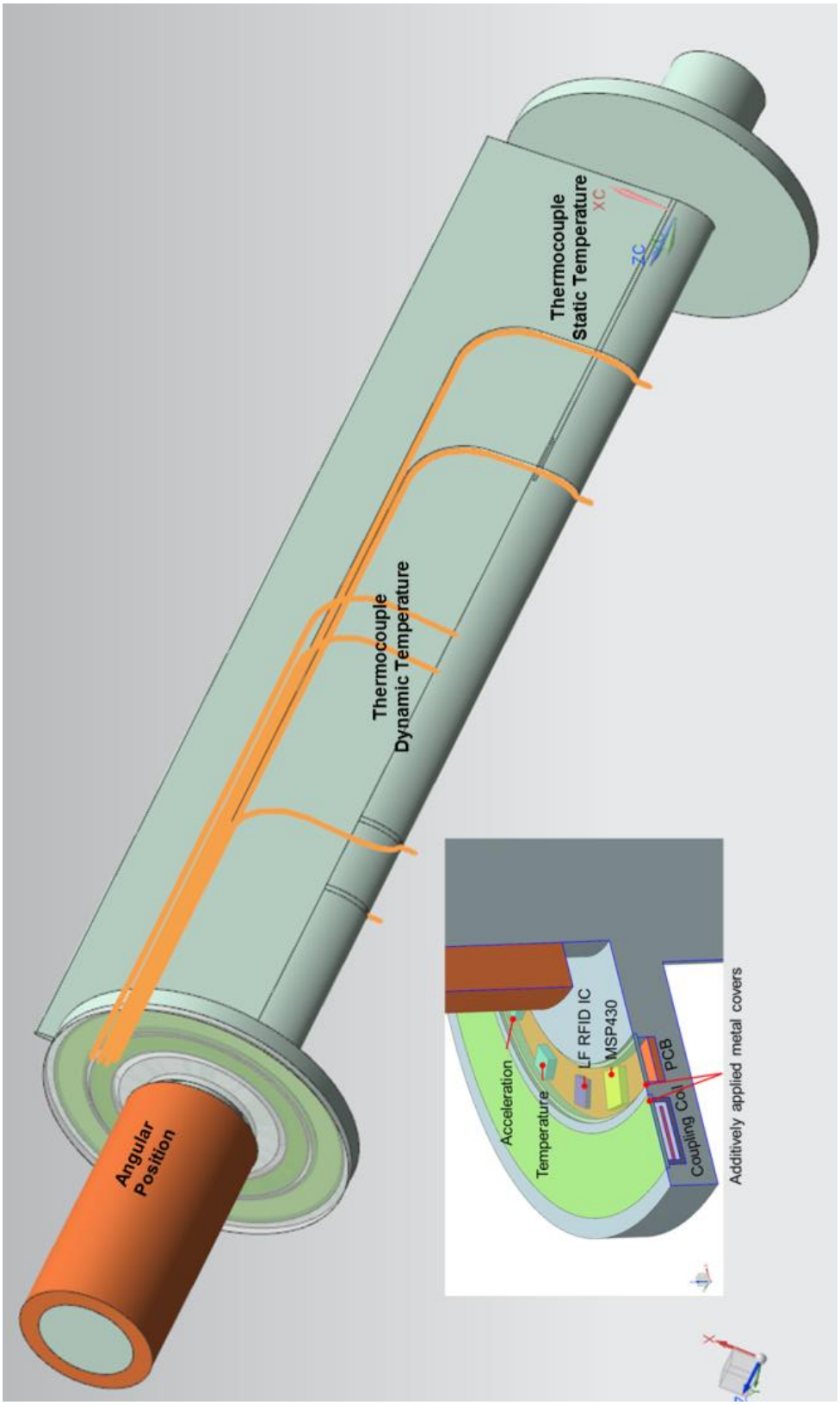
Thermocouple
Static Temperature
XC
ZC
Thermocouple
Dynamic Temperature
Angular
Position
Acceleration
Temperature
LF RFID IC
MSP430
PCB
Coupling Co
Additively applied metal covers

FIGURE 2

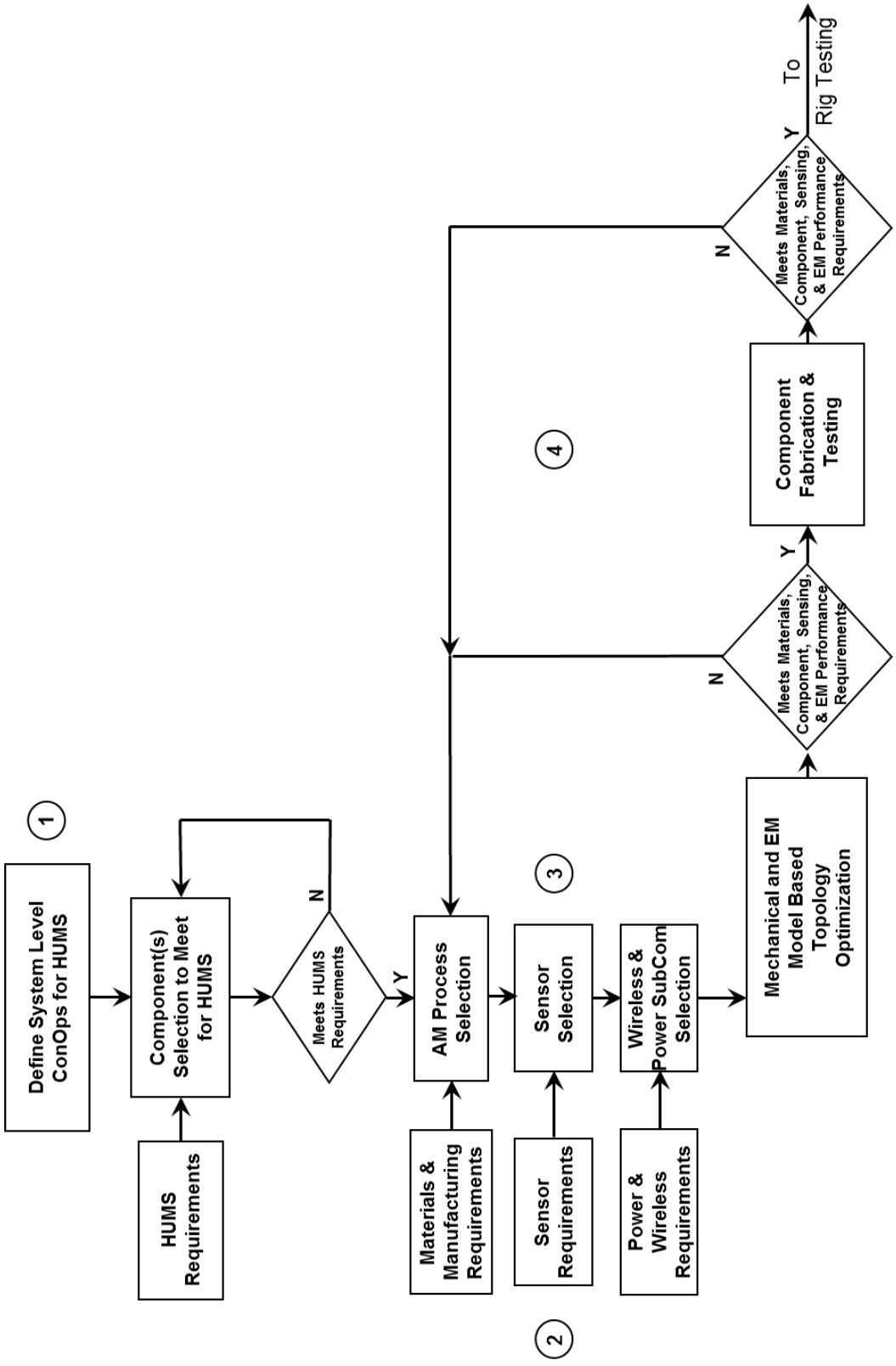
Define System Level ConOps for HUMS
Component(s) Selection to Meet for HUMS
HUMS Requirements
Meets HUMS Requirements
N
Y
AM Process Selection
Materials & Manufacturing Requirements
Sensor Selection
Sensor Requirements
Wireless & Power SubCom Selection
Power & Wireless Requirements
Mechanical and EM Model Based Topology Optimization
Meets Materials, Component, Sensing, & EM Performance Requirements
N
Y
Component Fabrication & Testing
Meets Materials, Component, Sensing, & EM Performance Requirements
N
Y
To Rig Testing
1
2
3
4

FIGURE 3

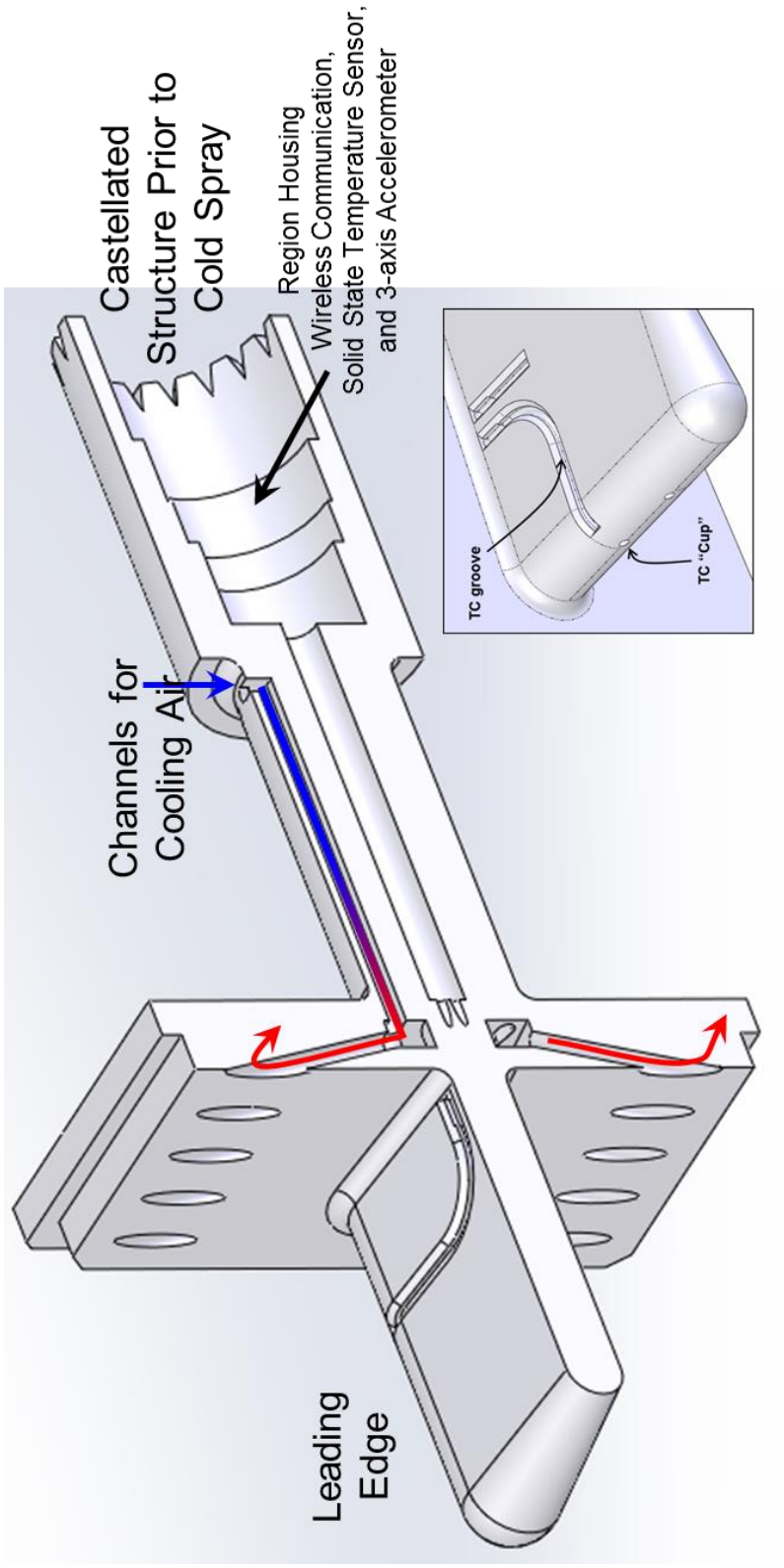
Castellated Structure Prior to Cold Spray
Region Housing Wireless Communication, Solid State Temperature Sensor, and 3-axis Accelerometer
Channels for Cooling Air
Leading Edge
TC groove
TC "Cup"

FIGURE 4a

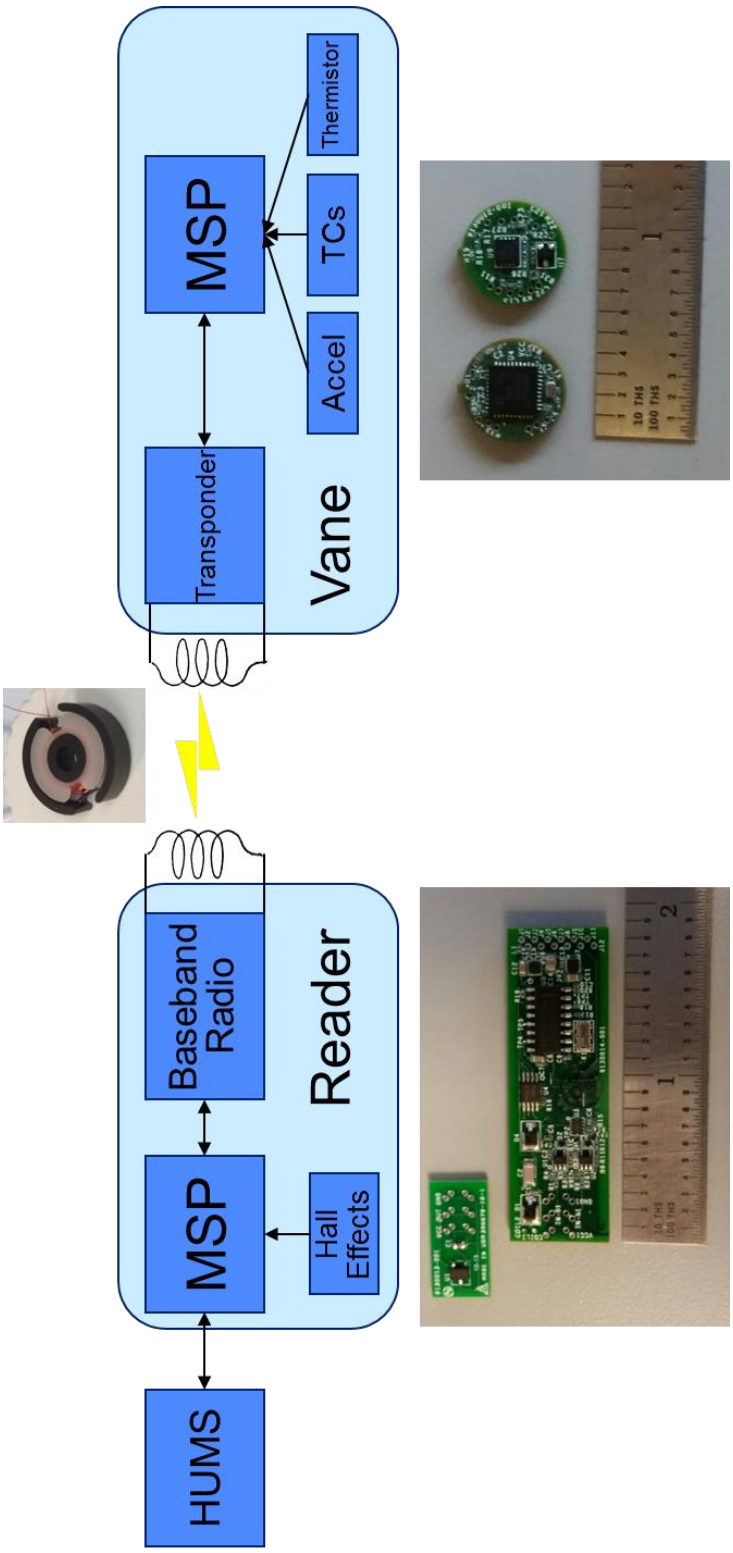
Thermistor
TCs
Accel
MSP
Transponder
Vane
Baseband Radio
MSP
Hall Effects
Reader
HUMS

FIGURE 4b

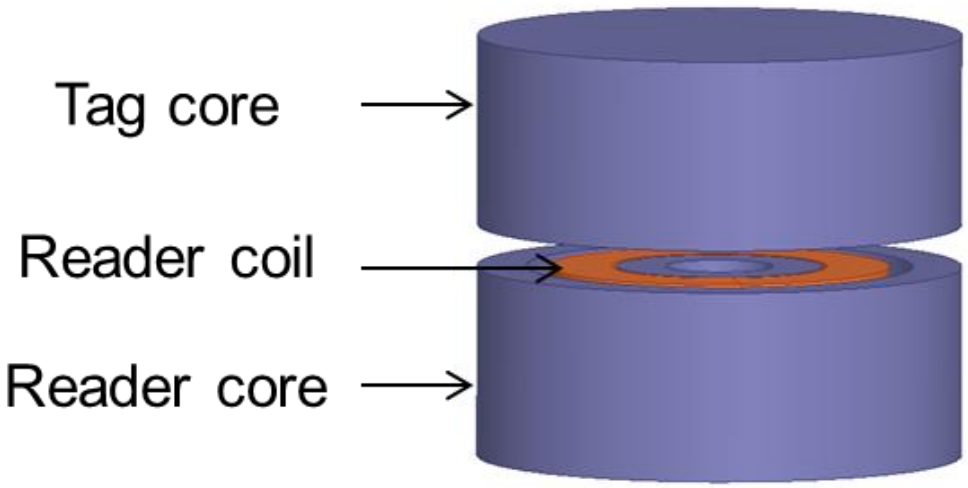

FIGURE 4c

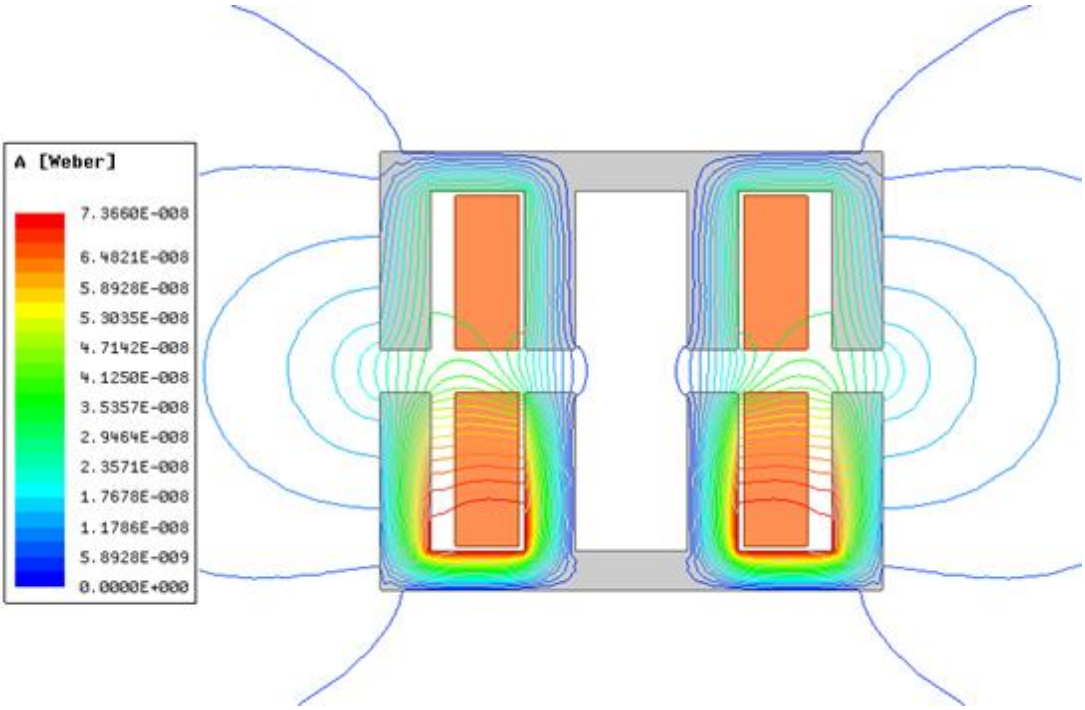
A [Weber]
7.3660E-008
6.4821E-008
5.8928E-008
5.3035E-008
4.7142E-008
4.1250E-008
3.5357E-008
2.9464E-008
2.3571E-008
1.7678E-008
1.1786E-008
5.8928E-009
0.0000E+000

FIGURE 5a

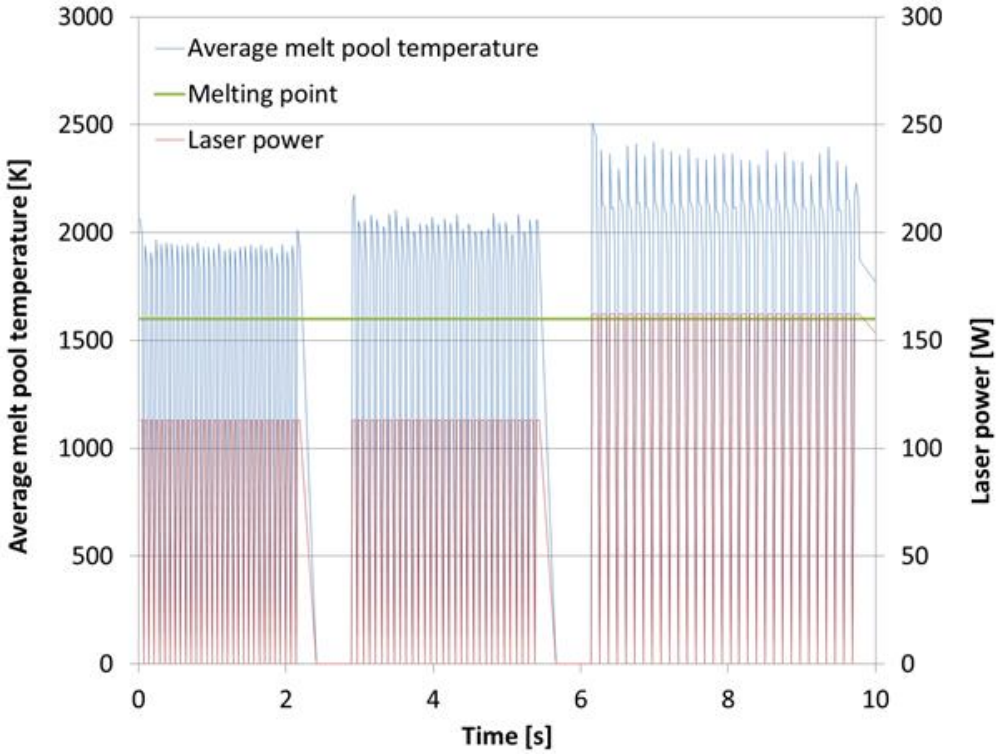
Average melt pool temperature
Melting point
Laser power
Average melt pool temperature [K]
Laser power [W]
Time [s]
3000
2500
2000
1500
1000
500
0
300
250
200
150
100
50
0
0
2
4
6
8
10

FIGURE 5b

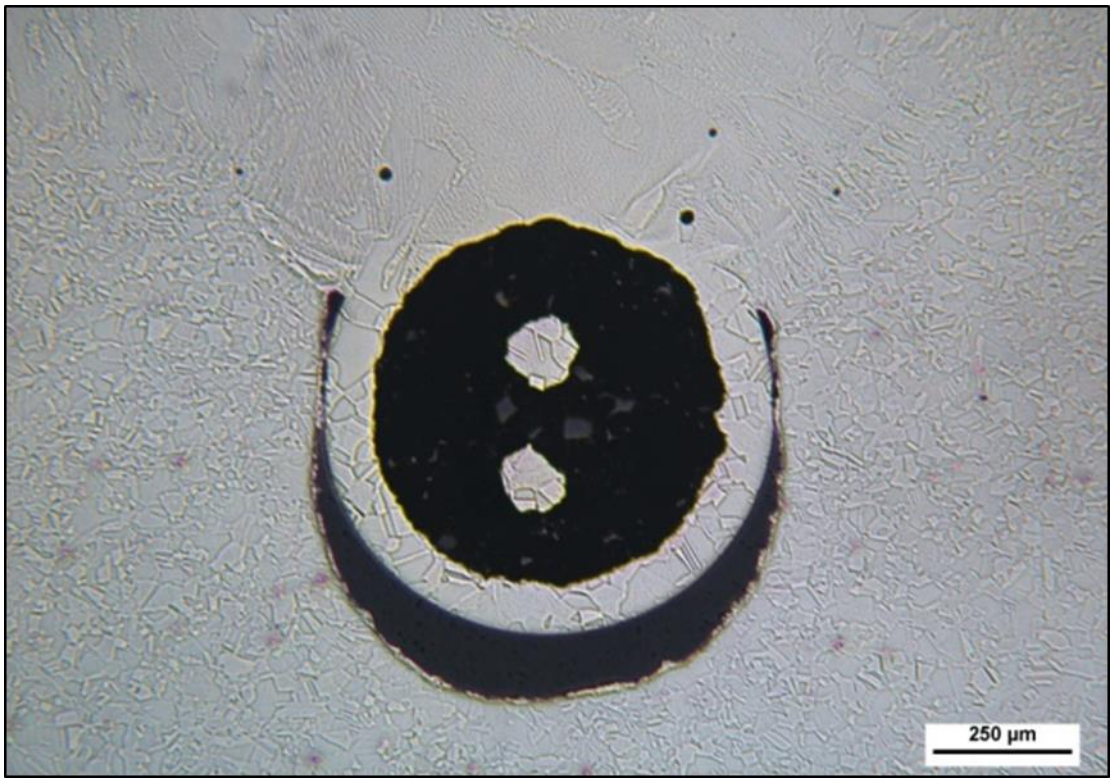

FIGURE 6a

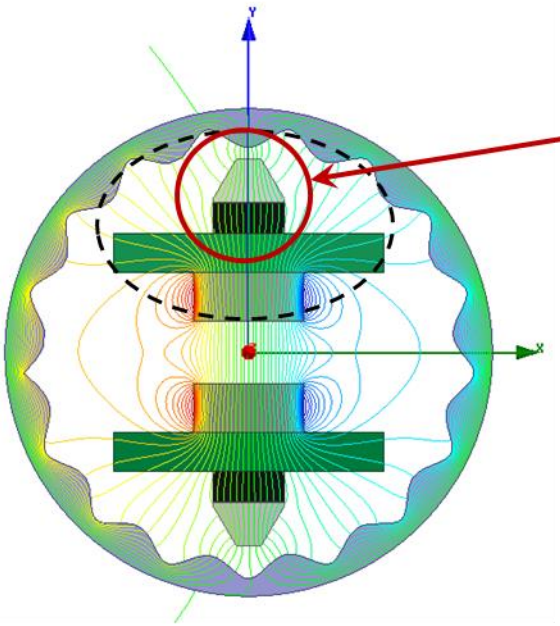

Flux Lines of the Variable Reluctance Sensing Assembly

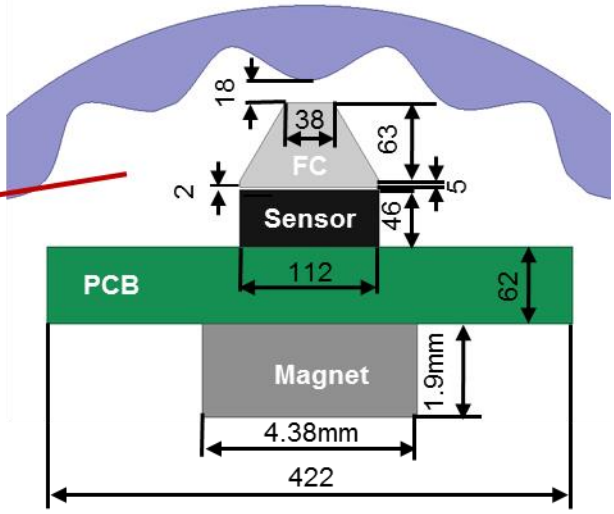

Design of Field Concentrator

*Unit: mil, unless otherwise noted

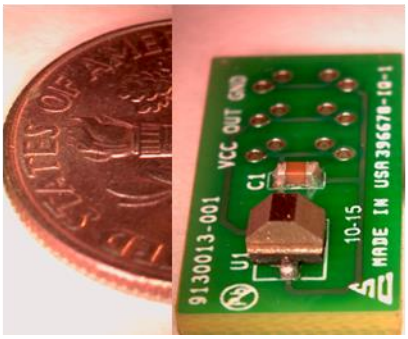

Board Level Assembly

FIGURE 6b

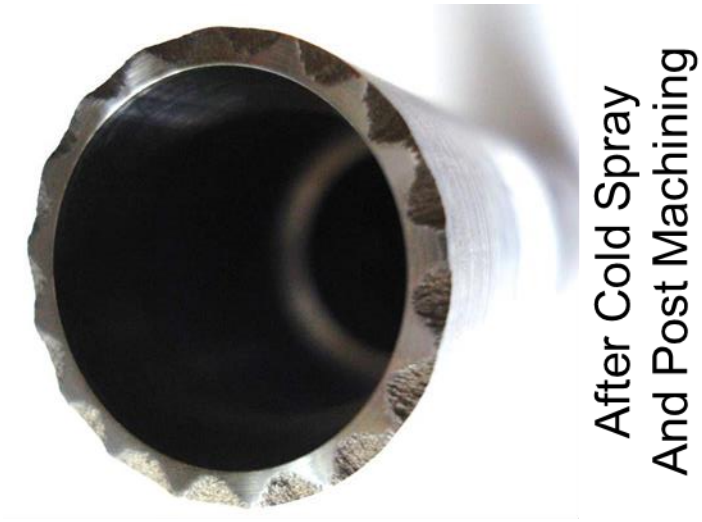

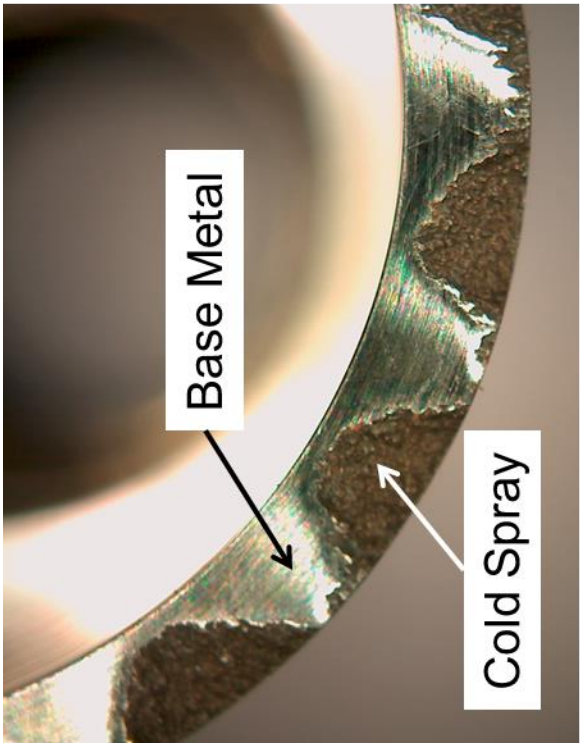

FIGURE 7

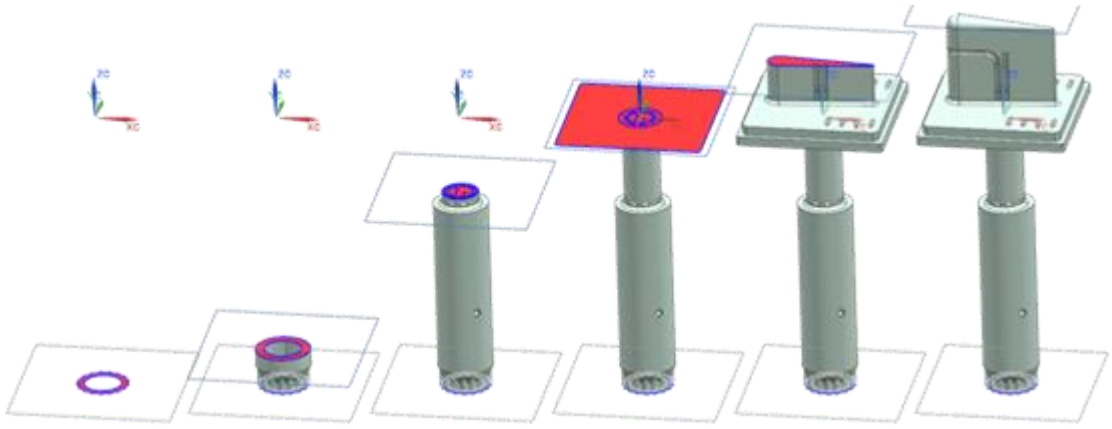

Flow Check Part
"Vane"

Cold Spray Demo
"Cup"

Reader Tip

FIGURE 8a

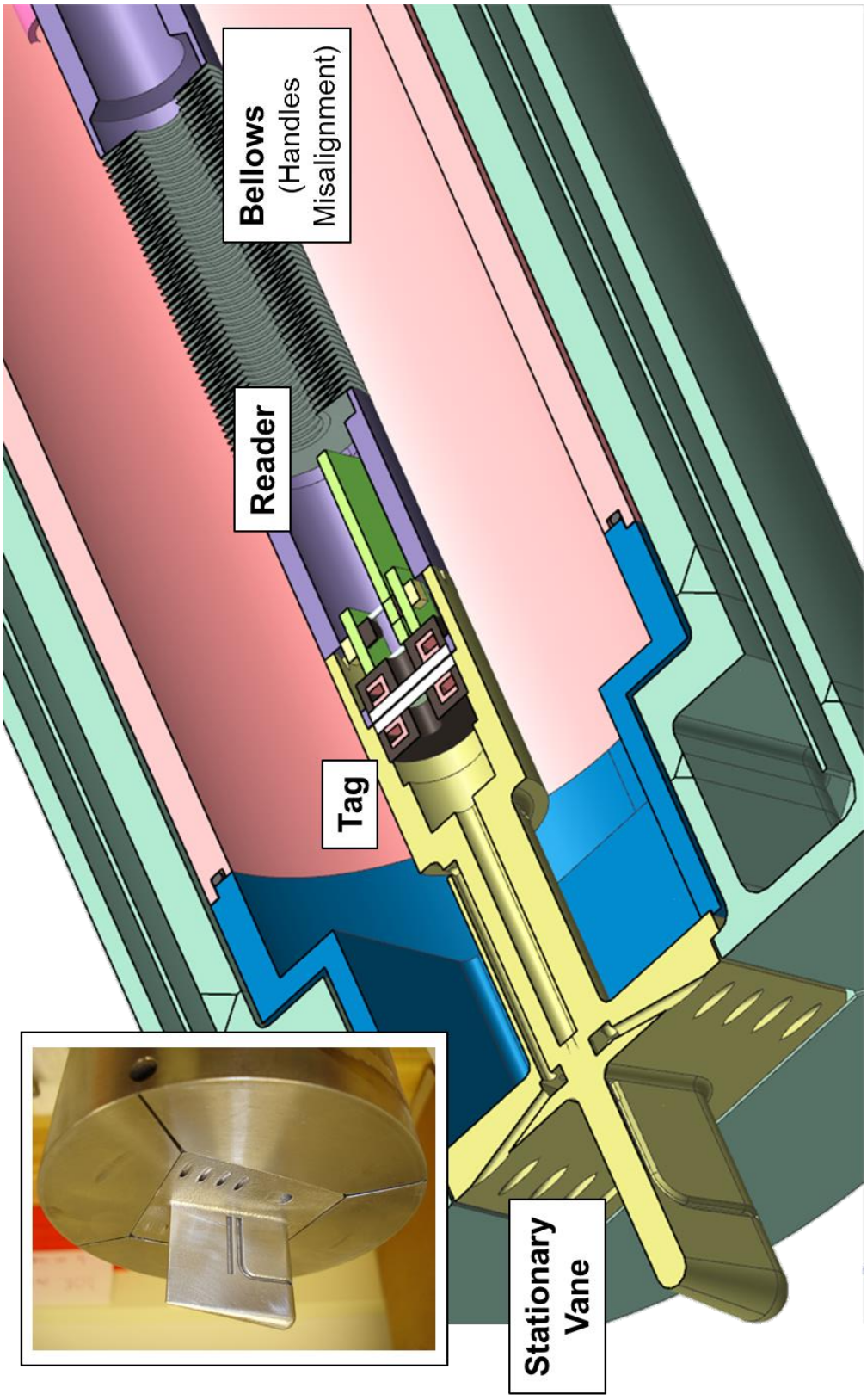

FIGURE 8b

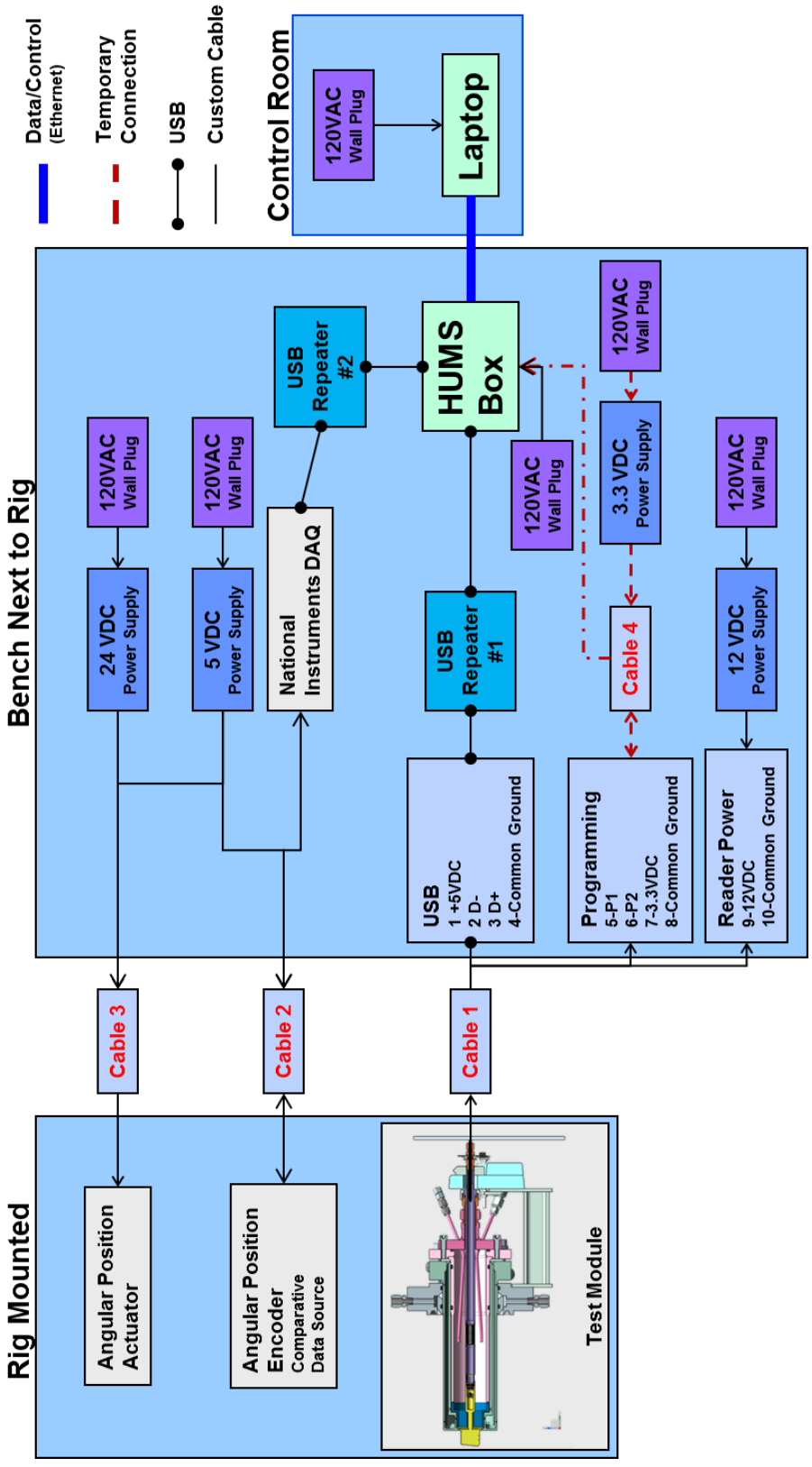
Data/Control (Ethernet)
Temporary Connection
USB
Custom Cable
Control Room
120VAC Wall Plug
Laptop
Bench Next to Rig
HUMS Box
USB Repeater #2
120VAC Wall Plug
3.3 VDC Power Supply
120VAC Wall Plug
24 VDC Power Supply
5 VDC Power Supply
National Instruments DAQ
USB Repeater #1
Cable 4
12 VDC Power Supply
120VAC Wall Plug
USB
1 +5VDC
2 D-
3 D+
4-Common Ground
Programming
5-P1
6-P2
7-3.3VDC
8-Common Ground
Reader Power
9-12VDC
10-Common Ground
Cable 3
Cable 2
Cable 1
Rig Mounted
Angular Position Actuator
Angular Position Encoder Comparative Data Source
Test Module

FIGURE 8c

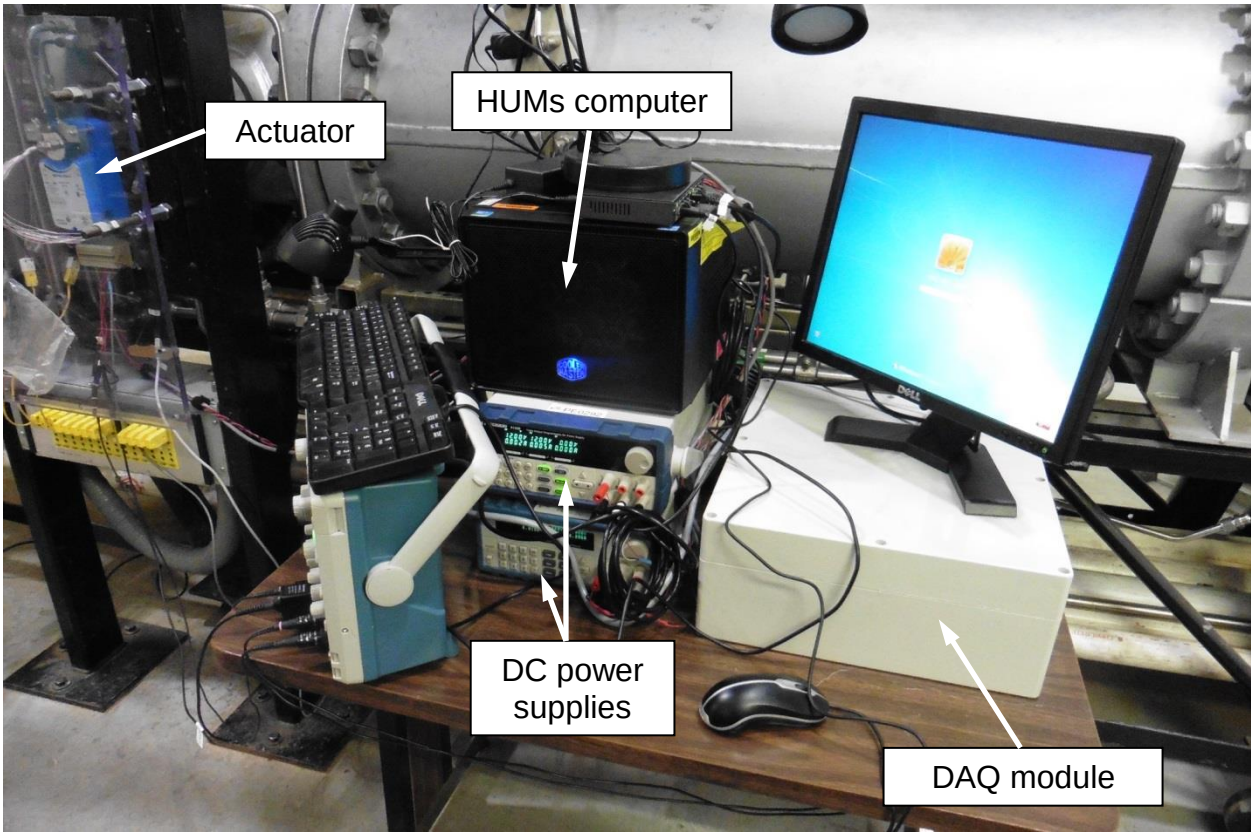

FIGURE 9a

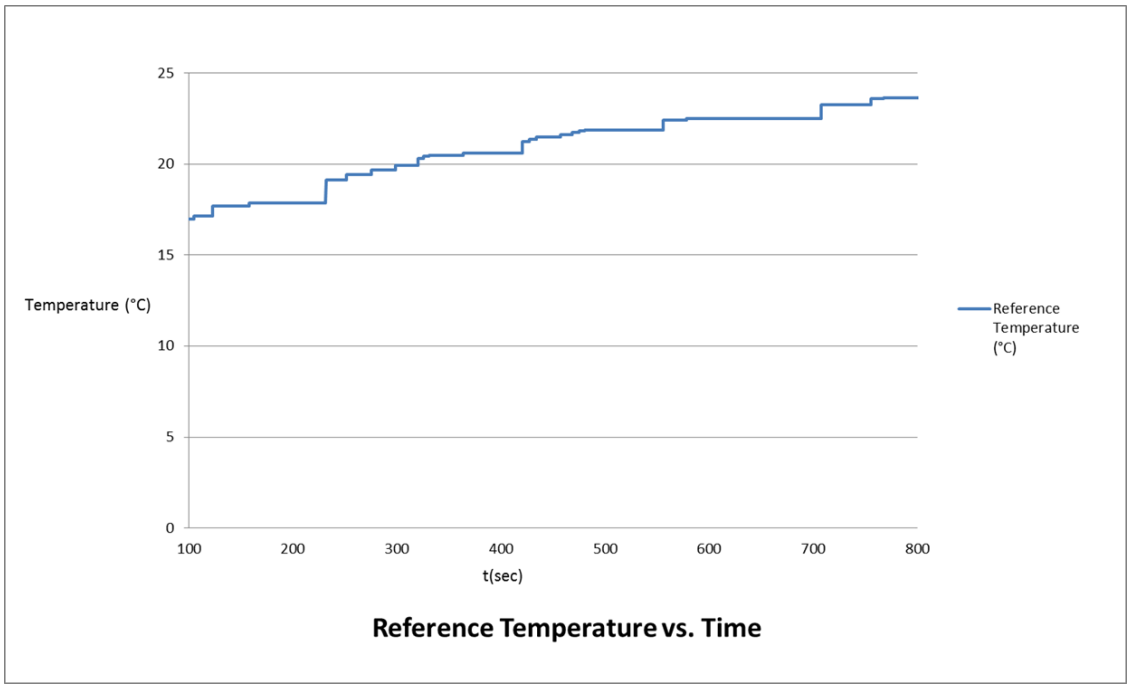
25
20
15
10
5
0
Temperature (°C)
100
200
300
400
500
600
700
800
t(sec)
Reference Temperature (°C)
Reference Temperature vs. Time

FIGURE 9b

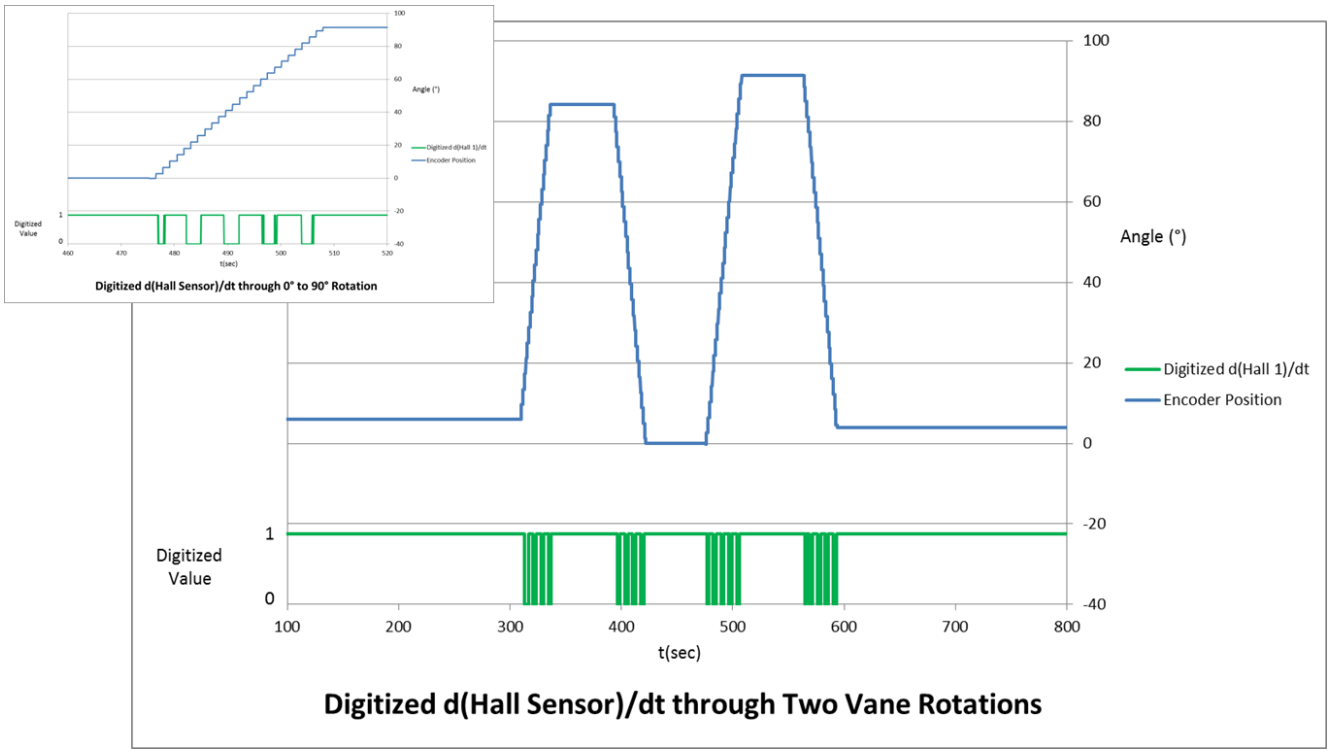
Digitized d(Hall Sensor)/dt through 0° to 90° Rotation
Digitized d(Hall Sensor)/dt through Two Vane Rotations
Angle (°)
Digitized d(Hall 1)/dt
Encoder Position
Digitized Value
t(sec)
100
80
60
40
20
0
-20
-40
1
0
100
200
300
400
500
600
700
800

FIGURE 9c

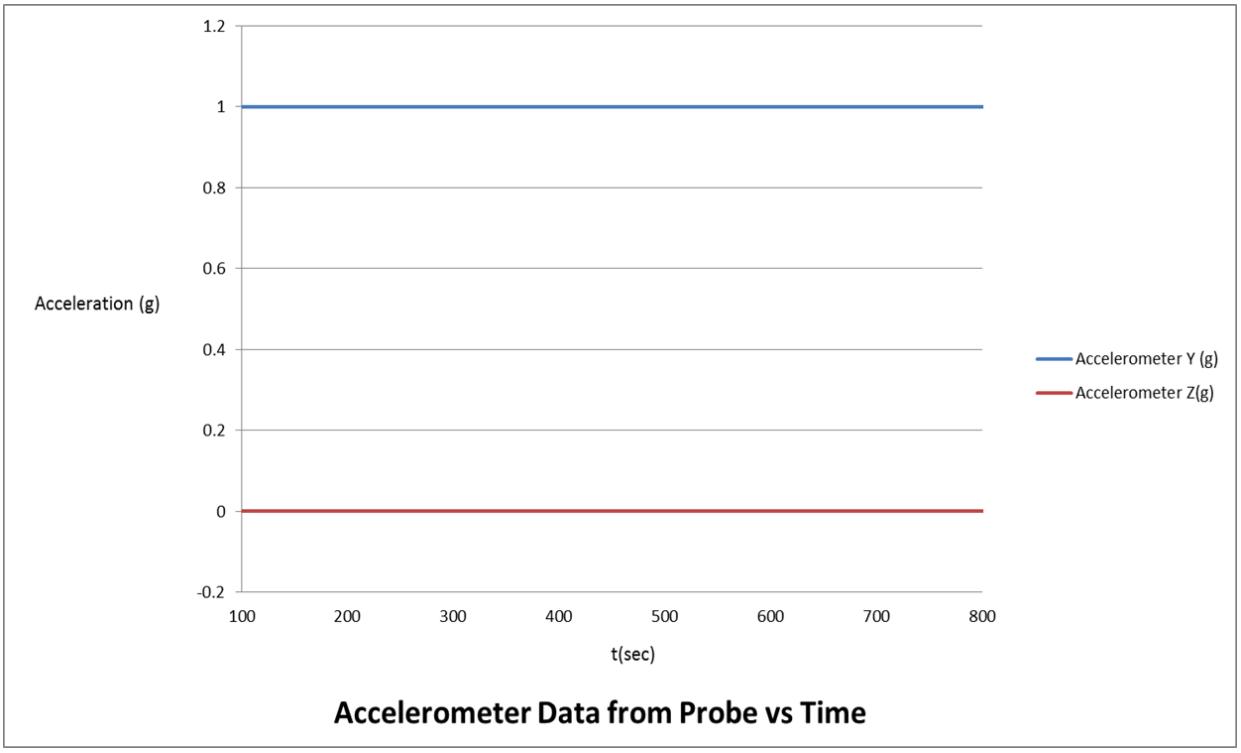
1.2
1
0.8
0.6
0.4
0.2
0
-0.2
Acceleration (g)
100
200
300
400
500
600
700
800
t(sec)
Accelerometer Y (g)
Accelerometer Z(g)
Accelerometer Data from Probe vs Time

FIGURE 9d

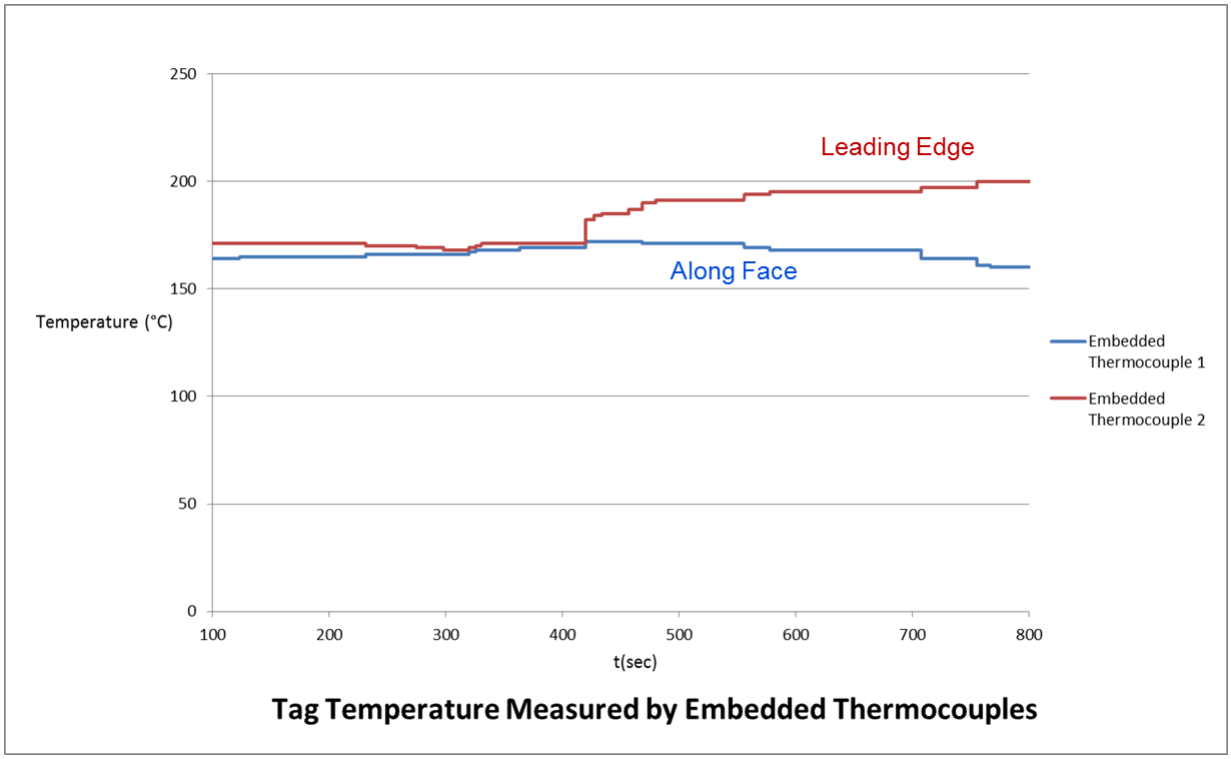
250
200
150
100
50
0
Temperature (°C)
100
200
300
400
500
600
700
800
t(sec)
Leading Edge
Along Face
Embedded Thermocouple 1
Embedded Thermocouple 2
Tag Temperature Measured by Embedded Thermocouples

FIGURE 9e

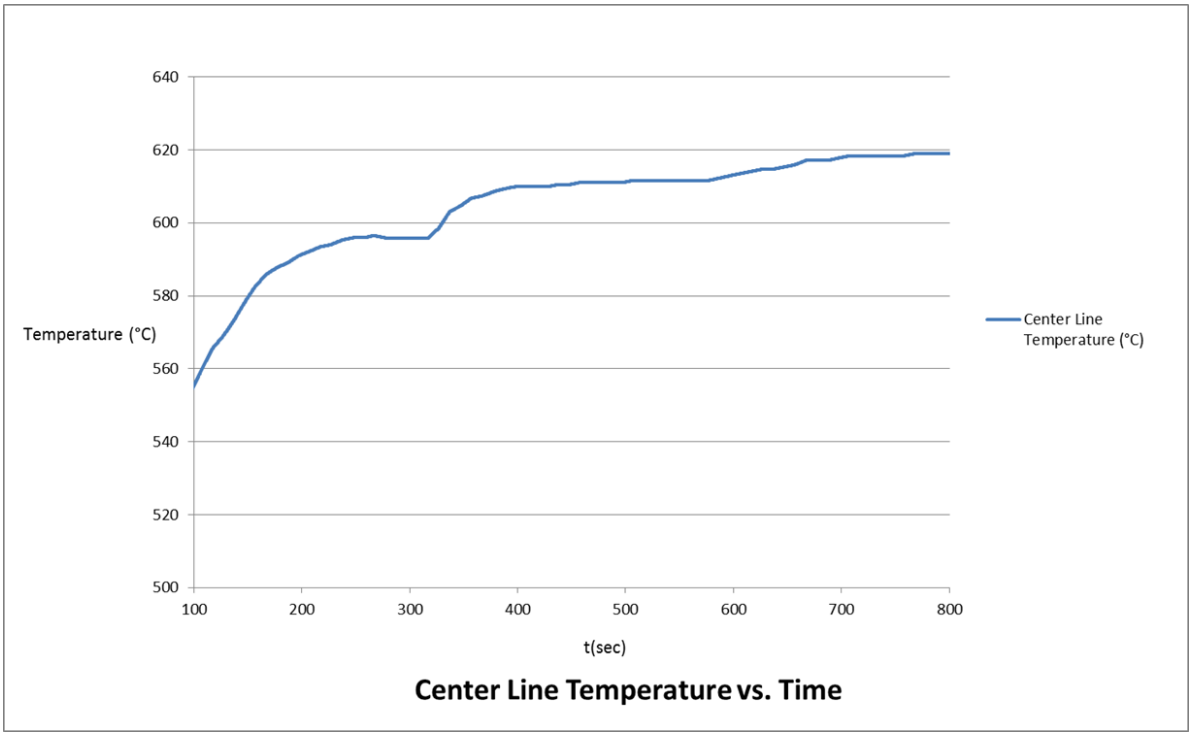
640
620
600
580
560
540
520
500
Temperature (°C)
100
200
300
400
500
600
700
800
t(sec)
Center Line Temperature (°C)
Center Line Temperature vs. Time

TABLE 1

Conditions	Leading Edge	Leading Edge	Slipstream	Reference	Metric
	74.0	74.0	73.4	74.2	°F
Room	23.3	23.3	23.0	23.4	°C
Temperature	0.2	0.1	0.1	0.1	mV
	33.5	33.5	32.9	32.8	°F
Ice	0.8	0.8	0.5	0.4	°C
Bath	1.0	1.0	1.0	1.0	mv
	124.4	125.5	124.4	125.6	°F
	51.3	51.9	51.3	52.0	°C
Transient #1	1.1	1.2	1.1	1.1	mV
	145.9	146.7	146.7	147.1	°F
	63.3	63.7	63.7	63.9	°C
Transient #2	1.6	1.6	1.6	1.6	mV
	206.4	208.7	209.7	208.6	°F
Boiling	96.9	98.2	98.7	98.1	°C
Water	2.9	3.0	3.0	3.0	mV